Interband optical transition spectra in GaAs quantum wires with rectangular cross sections

T. Sogawa,* H. Ando, S. Ando, and H. Kanbe
NTT Basic Research Laboratories, 3-1, Morinosato-Wakamiya, Atsugi-Shi, Kanagawa 243-01, Japan
(Received 25 November 1996; revised manuscript received 14 March 1997)

Interband optical transition spectra of rectangular GaAs quantum wires (QWR's) of various cross-sectional sizes are experimentally and theoretically studied. High-quality GaAs QWR's with lateral sizes below 20 nm are formed in AlAs trench structures with (110) vertical sidewalls by using metal-organic chemical vapor deposition. Polarization-dependent photoluminescence excitation (PLE) spectra in the QWR's clearly exhibit absorption peaks corresponding to optical transitions between quantized one-dimensional conduction and valence subbands. It is found that transition strengths and polarization anisotropies in the lowest- and higher-energy PLE peaks significantly vary, depending on the cross-sectional shape of the rectangular wires. The polarization-dependent interband transition matrix elements and the detailed absorption spectra are calculated by a multiband effective-mass theory considering heavy-hole and light-hole subband mixing. The theoretical results clarify the physical origin of observed PLE peaks and explain the strong dependence of interband transition properties on the cross-sectional ratio of QWR's. [S0163-1829(97)02128-0]

I. INTRODUCTION

Low-dimensional quantum nanostructures such as quantum wires (QWR's) and quantum dots (QDT's) have attracted considerable attention in view of their basic physics and potential device applications.[1,2] Various fabrication methods, such as fine etching of quantum-well (QW) structures and regrowth, growth on nonplanar substrates, growth on tilted substrates, selective growth on masked substrates, and overgrowth on cleaved-edge surfaces, have been demonstrated.[3–16] With these methods, QWR's and QDT's, which exhibit photoluminescence (PL) blueshifts and subband-energy separation due to quantum-confinement effects in the lateral (i.e., perpendicular to the growth axis) direction, have been fabricated. Recently, natural formation methods using multiatomic steps on vicinal substrates and the Stranski-Krastanow growth mode also have been actively investigated[17–20] because small QWR's and QDT's can be formed without the limitations of the lithographic technique. However, the achieved structures have a tendency to exhibit larger lateral sizes compared to the vertical (i.e., growth direction) thickness because of the poor size controllability in the lateral direction. Note that precise structural control as well as superior uniformity in QW structures is due to the fact that the structures are defined by the crystal planes, where layer-by-layer growth contributes to achieving atomic-scale control of flatness and thickness. An advanced technique utilizing crystal planes (or facets) is essentially required in order to control the shapes and sizes of multidimensional confinement structures on an atomic scale. The improved structure controllability can lead to a deep understanding of low-dimensional effects.

We previously reported on the fabrication of rectangular GaAs QWR's buried in AlAs trench structures with vertical (110) sidewalls by metal-organic chemical vapor deposition (MOCVD) on nonplanar GaAs substrates.[21–25] These QWR's, which we call ''trench-buried QWR's,'' have advantages in that the lateral width as well as the vertical thickness can be precisely controlled in the region below 20 nm by the growth process and that the abruptness of lateral interfaces between GaAs and AlAs layers is less than several monolayers.[23] Thus tight quantum confinement in two spatial dimensions can be achieved in trench-buried QWR's owing to their small sizes and to the large potential difference between the wires and the barrier layers. Polarization-dependent photoluminescence excitation (PLE) spectra that clearly exhibit not only the lowest, but also higher quantized transition peaks can be investigated in trench-buried QWR's, leading to the experimental exploration of one-dimensional (1D) band structures.

Several theoretical studies on 1D band structures have been reported, demonstrating that quantum confinement in two spatial dimensions significantly modifies valence-band structures; that is, that the heavy-hole (hh) and light-hole (lh) states are strongly mixed even at the zone center.[26–34] The PL and PLE spectra of the QWR's are therefore expected to exhibit strong polarization anisotropy, which is determined by the hh-lh mixing conditions. It has also been predicted that the valence-band structures as well as the hh-lh mixing conditions significantly depend on the cross-sectional shape of the QWR's, i.e., on the relative confinement strength between two confinement directions.[31] Thus the investigation into the cross-sectional shape dependence of overall absorption spectra including the lowest- and higher-energy transitions promises to offer important knowledge on the characteristics of 1D subbands in quantum-wire structures.

This paper reports on our systematic study of interband optical transition spectra in GaAs/AlAs rectangular QWR's with various cross-sectional sizes. The polarization-dependent PLE spectra clearly exhibit quantized transition peaks, demonstrating anisotropic optical transition properties determined by the characteristics of 1D valence subbands. It is also revealed that the transition strength, polarization anisotropy, and quantized energy of each transition vary with the change in the cross-sectional shape of the QWR's. We analyze theoretically interband transition properties in rectangular QWR's using the multiband effective-mass theory, which takes the mixing of the hh and lh states into account.

The transition matrix elements between conduction and valence subbands for different polarization conditions with respect to the wire direction are derived to facilitate discussion of the experimental results. We also calculate the detailed absorption spectra by considering the k dependence of the transition matrix element. The theoretical results clarify the physical origin of the observed PLE peaks and explain the strong dependence of the interband transition properties on the cross-sectional ratio of the QWR's, confirming the formation of 1D valence-subband structures that significantly depend on quantum confinement conditions, i.e., on relative confinement strength between two directions.

The remainder of the article is organized as follows. Section II describes the fabrication method for rectangular GaAs/AlAs QWR's. Section III shows PL and PLE spectra for QWR's of various wire sizes. In Sec. VI the transition matrix element and absorption spectra for rectangular QWR's are calculated. The valence-band structures are analyzed by using a multiband effective-mass method that treats hh-lh mixing. The theoretical model is described in Sec. VI A. In Sec. VI B we show the polarization dependence of the transition matrix element between 1D conduction and valence subbands to discuss optical transition properties. The numerically calculated absorption spectra of rectangular QWR's with various cross-sectional ratios are also presented. In Sec. VI C we discuss the experimental results in comparison with the calculated transition properties. Section V summarizes our conclusions.

II. FABRICATION METHOD FOR RECTANGULAR QUANTUM WIRES

Figure 1 shows schematically the process employed in the fabrication of the GaAs/AlAs rectangular QWR's. The first step is substrate patterning. The (001) GaAs substrates are patterned with V-shaped grooves oriented along the ⟨110⟩ direction, using electron-beam lithography (JEOL 6000FS) and wet chemical etching. We formed 150-nm-pitch gratings composed of 600 grooves, where the sidewalls of the V-shaped grooves are (111)A facets. Low-pressure (76 torr) MOCVD growth using trimethylgallium, trimethylaluminum, and arsine were applied. An AlAs layer initially grown on the V-shaped grooves produces trench structures with vertical sidewalls.[21–25] The sidewalls correspond to (110) facets perpendicular to the (001) substrate. We observed that the trench structures can be formed when the growth temperature is 620 –650 °C and the group V/III ratio for AlAs growth is 110–220. We have reported that the trench width between the opposite sidewalls is determined by the growth conditions, i.e., by a combination of the growth temperature and the group V/III ratio for AlAs growth.[22,23] The trench width becomes about 20 nm when the growth temperature is 620 °C and the V/III ratio is 220, whereas the trench width becomes about 30 nm when the growth temperature is 650 °C and the V/III ratio is 110. Since the lateral growth rate on the (110) facets is slow, an increase in the AlAs growth time does not effectively reduce the trench width below the growth-condition-determined dimensions of 20–30 nm. To further reduce the trench width, GaAs/AlAs short-period superlattice layers (SL's) were grown after the formation of the base AlAs trenches because GaAs/AlAs short-period SL's can laterally grow on (110) facets. The difference of the growth mechanism between the AlAs layer and GaAs/AlAs SL's on (110) facets will be discussed elsewhere. By changing the number of SL's or the thicknesses of GaAs or AlAs layers in the SL's, the trench width can be precisely controlled. The next step is the growth of GaAs wires inside the trenches. As a result of the migration of Ga species into the trenches, the GaAs growth rate at the bottom of the trenches is enhanced compared to the growth rate on planar substrates. We found that the GaAs wire thickness is proportional to the supplied thickness and that the enhancement factor is determined by the growth condition.[21] Thus the thickness of the GaAs wires can be precisely controlled by changing the GaAs growth time. The final step is growth of the upper barrier layer, where AlAs, $Al_xGa_{1-x}As$, or GaAs/AlAs SL's can be chosen.[23]

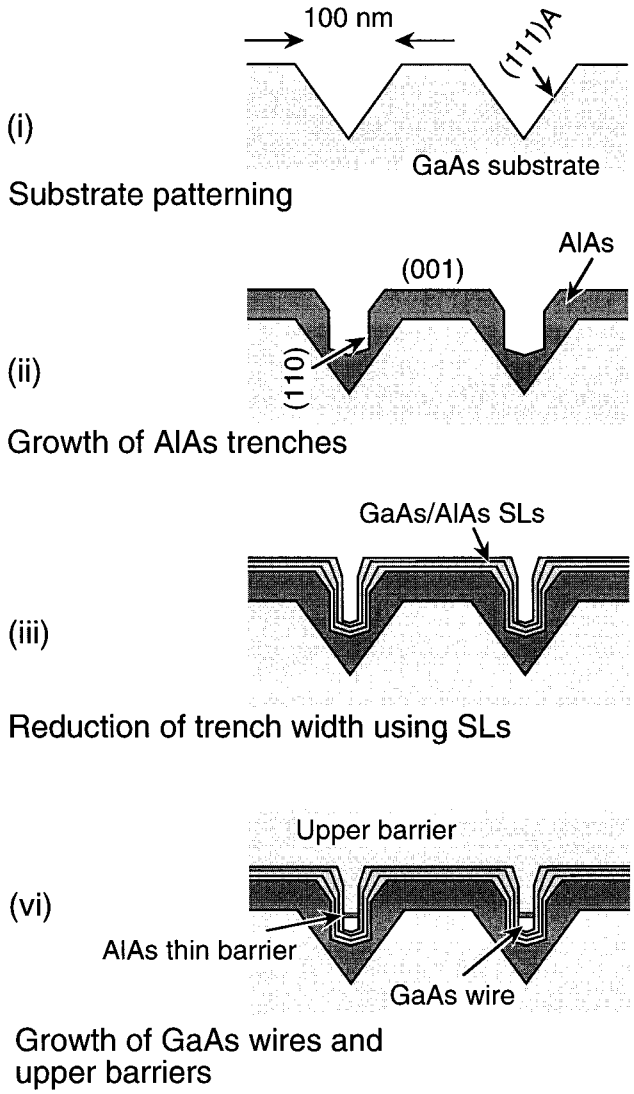

FIG. 1. Schematic illustrations of the fabrication process of GaAs/AlAs rectangular QWR's.

Figure 2 shows a transmission electron microscopy bright-field image for the cross section of a typical trench-buried QWR that includes the narrowing SL's. The dark and bright spots correspond to the GaAs and AlAs lattice images, respectively, exhibiting a 13-nm-wide and 13-nm-thick nearly square GaAs QWR surrounded by barrier layers with

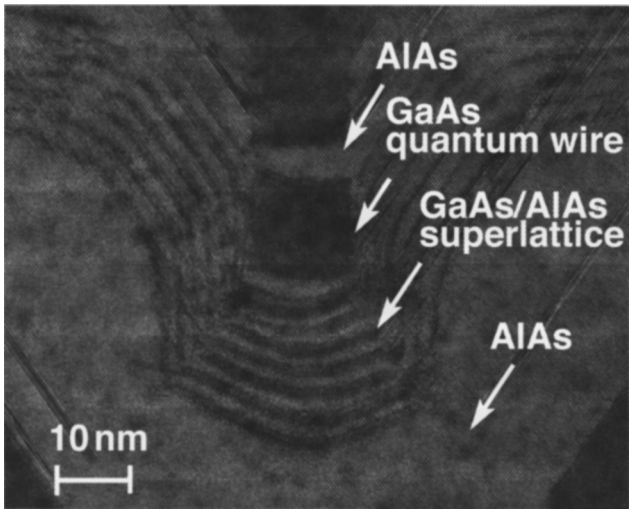

FIG. 2. Transmission electron microscopy bright-field image for the cross section of a typical trench-buried QWR that includes narrowing SL's. Dark and bright spots correspond to the GaAs and AlAs lattice images, respectively.

an interface roughness of several monolayers. The structure consists of an AlAs (23-nm) layer; seven pairs of GaAs/AlAs (0.8-nm/2-nm) SL's, where the top AlAs layer is 4 nm thick; a GaAs (2-nm) layer; a thin AlAs (4-nm) barrier layer; and a thick $Al_{0.4}Ga_{0.6}As$ cover layer. These thicknesses correspond to those on the planar substrate. This sample was grown at a growth temperature of 650 °C with a group V/III ratio of 110 for AlAs growth. Under this growth condition, the growth-condition-determined trench width is about 30 nm. The layered structures of the SL's can be seen at the bottom and sidewalls, demonstrating that the growth of SL's can reduce the lateral width from 30 to 13 nm.

For measurement of PLE spectra in rectangular QWR's, we prepared four kinds of QWR's with different wire sizes (samples 1–4). Table I shows the widths and thicknesses for samples 1–4 evaluated by TEM observation. Here we chose a growth temperature of 620 °C and a group V/III ratio of 220 for AlAs growth in order to prevent the incorporation of carbon impurities by increasing As coverage on the growing surfaces. The reduction of residual impurities is important in the study of band structures through PLE properties because band-edge structures disappear due to band-filling effects, as will be discussed elsewhere.[35] Under this growth condition, the growth-condition-determined trench width is about 20 nm.[21] Samples 1–3 are composed of a 20-nm-wide AlAs trench, GaAs wires, and an upper AlAs barrier layer. The thicknesses of GaAs wires of samples 1–3 were designed to be about 16, 13, and 11 nm, respectively, by changing the GaAs growth time. Only sample 4 had five pairs of thin GaAs/AlAs (0.4-nm/1-nm) SL's that were successively grown on 20-nm-wide base AlAs trenches. The last AlAs layer in the SL's is 4 nm thick. The SL's reduce the trench width to 16–17 nm. The GaAs wires were designed to be about 10 nm thick. The wave functions are tightly confined within the GaAs wire regions in all samples due to the large energy difference between the GaAs wire regions and the surrounding barrier regions.

TABLE I. Structure parameters of QWR samples.

Sample	Lateral width (nm)	Vertical thickness (nm)
1	20	16
2	20	13
3	20	11
4	17	10

III. POLARIZATION-DEPENDENT PLE SPECTRA OF RECTANGULAR QUANTUM WIRES

Figures 3(a)–3(d) show the low-temperature (15-K) PL and PLE spectra for samples 1–4, respectively. A few milliwatts of Ti:sapphire laser light with a spot size of 100 μm was used for excitation. The dotted lines represent the PL spectra. The solid circles and open circles are the PLE spectra obtained with incident polarization (light electric-field vector) parallel and perpendicular to the wires, respectively. The incident light is traveling parallel to the epitaxial growth direction. The PLE spectra in all samples have clear peak structures corresponding to optical transitions between quantized conduction and valence subbands, as indicated by the arrows. It is observed that each peak exhibits strong polarization anisotropy. The lowest-energy and third energy PLE peaks appear for parallel polarization, the second peak appears for perpendicular polarization, and the fourth peak (shoulder) appears for both polarizations. The peak positions are found to vary with changes in the wire size. It should also be noted that the shapes of the PLE spectra, such as peak intensity and the degree of polarization anisotropy at each transition peak, vary with the samples. In Figs. 3(a)–3(c), which show the changes in the PLE spectra as a function of the wire thickness, the second PLE peak becomes smaller compared to the intensity of the first peak and the third peak prominently appears as the thickness of the QWR's becomes thinner. Samples 2 and 4, which have almost the same cross-sectional ratio, exhibit similar PLE spectra except for the difference in the energetic positions of the peaks. These results clearly demonstrate that the characteristics of valence-band structures, which determine the transition strength and polarization anisotropy, significantly depend on the cross-sectional ratio of QWR's. The origin of each PLE peak will be discussed theoretically in Sec. VI

In Figs. 3(a)–3(d) the lowest PLE peaks are Stokes shifted by 15–30 meV, which is comparable with PL inhomogeneous broadening for each sample. We ascertained that the energetic positions of the lowest- and higher-energy PLE peaks do not sensitively depend on the detecting photon energy of PLE measurement. The Stokes shifts are therefore attributed to the nonuniformities along the wire direction. It should also be noted that the QWR's used in the present study were slightly doped due to the residual carbon impurities incorporated during growth.[35] The hole concentration was estimated not to be sufficiently high to modify the valence-band structures. However, we have to take into account that the phase-space filling and screening effects due to the residual holes reduce the excitonic binding energy. When the background carrier concentration is very low, the excitonic binding energy is estimated to be 10–20 meV for 20-

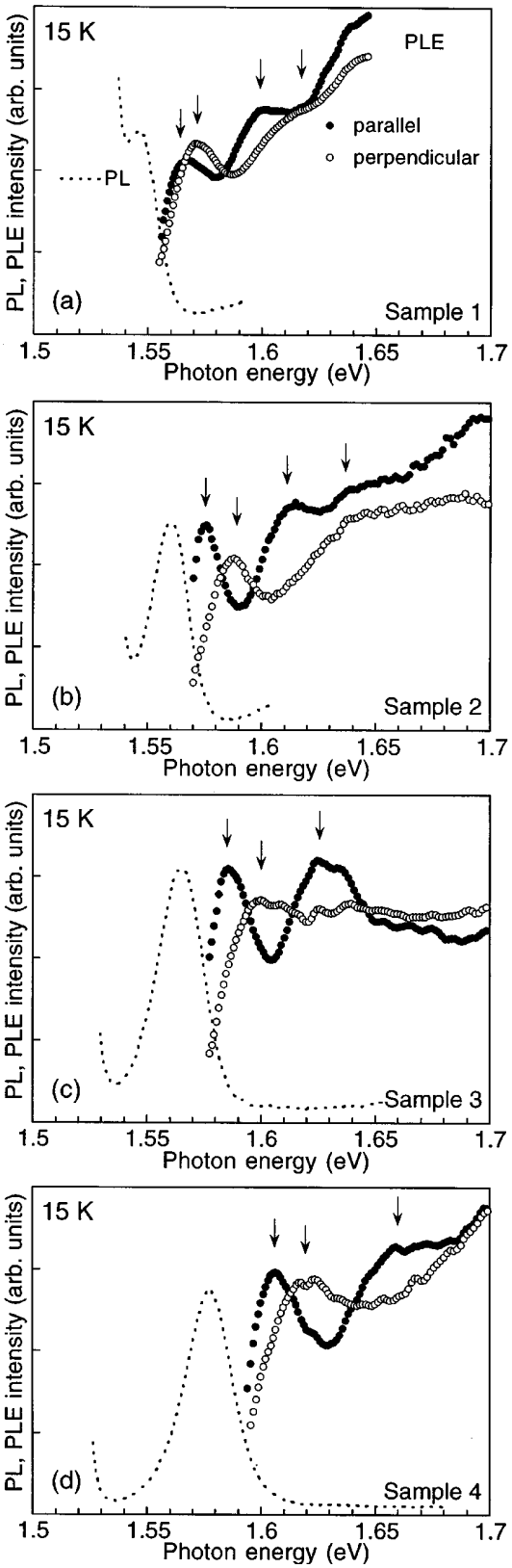

FIG. 3. Low-temperature (15 K) polarization-dependent PLE spectra and PL spectra for (a) sample 1 ($20\times16\ \mathrm{nm}^2$), (b) sample 2 ($20\times13\ \mathrm{nm}^2$), (c) sample 3 ($20\times11\ \mathrm{nm}^2$), and (d) sample 4 ($17\times10\ \mathrm{nm}^2$). The dotted lines indicate the PL spectra. The solid circles and open circles represent the PLE spectra obtained with incident polarization parallel and perpendicular to the wires, respectively. The incident light travels parallel to the epitaxial growth direction.

nm-wide QWR's.[31,36–38] In this case, the transition spectrum has pronounced excitonic transitions and suppressed interband transitions because the strong Coulomb interaction concentrates the oscillator strength into the excitonic transitions from interband transitions.[31,38] On the other hand, the reduced excitonic effects due to the residual carriers cause the decrease of the excitonic transitions and recovery of the interband transitions. Note that in the 1D system the oscillator strength conservation rule holds near the band-edge region because of the inverse-square-root dependence of the density of states. Since the excitonic binding energies are obviously below the inhomogeneous broadening of 15–30 meV in the present experimental conditions, it is unclear whether the observed peak structures are due mainly to the excitonic transitions or to the interband transitions reflecting the inverse-square-root-type density of states. It should be emphasized that polarization properties of the excitonic transitions strictly reflect the characters of the valence subbands forming the excitonic states.[31] Thus, even if the excitonic effects are not negligible, the main features of the transition spectra are considered to be similar to the calculated interband absorption spectra in the QWR's with a smaller excitonic binding energy than the inhomogeneous broadening. From the above reasons, we will discuss the experimental results based on the interband optical transition spectra by considering the characteristics of 1D valence subbands in the next section.

IV. INTERBAND OPTICAL TRANSITION SPECTRA OF RECTANGULAR QUANTUM WIRES

A. Calculation model and method

Our theoretical discussion on interband transition properties begins with an analysis of electron and hole states that are confined in the rectangular GaAs wire region (with a lateral width of L_x and vertical thickness of L_z) surrounded by infinite potential barriers.[31] Since we deal with the optical transitions near the fundamental GaAs band-gap energy, we can assume that the conduction and valence bands are decoupled and can neglect the effects of split-off bands. A simple effective-mass model can be used to describe the electron states in the conduction band. The conduction-band wave functions $\psi^{(m,n)}_{m_s,k}(\mathbf{r})$ are written as

$$\psi^{(m,n)}_{m_s,k}(\mathbf{r})=\frac{2}{\sqrt{L_xL_z}}\sin\frac{\pi mx}{L_x}\sin\frac{\pi nz}{L_z}\exp(-iky)u^c_{m_s}, \tag{1}$$

where the $u^c_{m_s}$ are the two spin-degenerate ($m_s=\pm1/2$) Bloch functions at the bottom of the Γ_6 bulk band, m and n refer to the indices of the envelope component in the x and z directions, and k is the wave vector in the y (wire) direction. On the other hand, valence-subband states can be analyzed with the Luttinger-Kohn 4×4 Hamiltonian H^v,[39,40] modified by Bockelmann and Bastard.[29] The valence-band wave functions $\psi^l_k(\mathbf{r})$ are expanded by using an orthogonal function set[31]

$$\psi_k^l(\mathbf{r}) = \frac{2}{\sqrt{L_x L_z}} \sum_{m,n} \sum_{m_j} J_{k,m_j}^{l-(m,n)} \sin\frac{\pi m x}{L_x} \sin\frac{\pi n z}{L_z} \times \exp(-iky) u^v_{m_j}, \quad (2)$$

where $u^v{}_{m_j}$ ($m_j = \pm 3/2$ and $\pm 1/2$) represents the degenerate Bloch functions at the top of valence band (Γ_8) and the suffix l refers to the index of the 1D valence subband numbered from the top of the valence band at $k=0$. Substituting the expanded wave function (2) into the matrix equation $[H^v - E_v^l(k)]\psi_k^l(\mathbf{r}) = 0$, we have the secular equation of a 4 mn×4 mn real matrix to be solved for the eigenenergy $E_v^l(k)$ and eigenvector $J_{k,m_j}^{l-(m,n)}$ of each valence-subband state.[31]

The optical transition probability can be discussed based on the squared transition matrix element of a transition between the lth valence subband v_l and the conduction subband $c_{m,n}$, which comprises the electron state with the (m,n) envelope. The squared transition matrix element is given[29] as

$$|M_k^{l-(m,n)}|^2 = \sum_{m_s} |\langle \psi_{m_s,k}^{(m,n)} | \boldsymbol{\varepsilon}\cdot\mathbf{p} | \psi_k^l \rangle|^2 = K_k^{l-(m,n)} |\langle c|p|v\rangle|^2, \quad (3)$$

$$K_k^{l-(m,n)} = \frac{1}{2}(|J_{k,3/2}^{l-(m,n)}|^2 + |J_{k,-3/2}^{l-(m,n)}|^2) + \frac{1}{6}(|J_{k,-1/2}^{l-(m,n)}|^2 + |J_{k,l/2}^{l-(m,n)}|^2) \pm \frac{1}{\sqrt{3}}(J_{k,3/2}^{l-(m,n)} J_{k,-l/2}^{l-(m,n)} + J_{k,l/2}^{l-(m,n)} J_{k,-3/2}^{l-(m,n)}) \begin{pmatrix} +:\varepsilon\|y \\ -:\varepsilon\|x \end{pmatrix}, \quad (4)$$

where $\boldsymbol{\varepsilon}$ is the polarization vector of the light, $|\langle c|p|v\rangle|^2$ corresponds to the transition probability of the GaAs bulk, and $K_k^{l-(m,n)}$ expresses the polarization-dependent factor in the squared transition matrix element. The signs + and − in the third term of Eq. (4) correspond to the polarization vector parallel and perpendicular to the wire axis, respectively. Polarization-dependent absorption spectra are obtained by using the squared transition matrix element and the joint density of states.

B. Polarization dependence of transition matrix element and absorption spectra in rectangular QWR's

Figures 4(a)–4(d) show the numerically calculated absorption spectra and the values of $K_{k=0}^{l-(m,n)}$ at each transition edge ($k=0$) for rectangular QWR's with cross-sectional ratios of (a) $L_x/L_z = 10/9$, (b) $L_x/L_z = 4/3$, (c) $L_x/L_z = 3/2$, and (d) $L_x/L_z = 2/1$. The solid lines and dashed lines in the upper part of each figure represent the absorption spectra for incident polarization (light electric-field vector) parallel and perpendicular to the wires, respectively. Solid (hatched) bars in the lower part of each figure show the values of $K_{k=0}^{l-(m,n)}$ for the electric field parallel (perpendicular) to the wires. In this calculation, the electron effective mass of $m_e^* = 0.067 m_0$, where m_0 is the electron rest mass, and Luttinger parameters of $\gamma_1 = 7.21$ and $\gamma_2 = \gamma_3 = 2.49$ are used. These Luttinger parameters give the hh and lh effective masses of $0.45 m_0$ and $0.11 m_0$, respectively, in the GaAs bulk. The vertical axis shows the absorption intensity normalized for the wire cross section. The horizontal axis is the sum of the conduction- and valence-subband confinement energies normalized by $\pi^2\hbar^2/2m_0L_x^2$. The unit scale of the horizontal axis corresponds to 0.94 meV when $L_x = 20$ nm. The label v_l-$c_{m,n}$ denotes a transition between the v_l valence subband and the $c_{m,n}$ conduction subband with the (m,n) envelope. Since each valence subband consists of various (m,n) envelope states, the $c_{m,n}$ conduction subband can optically couple with many valence subbands according to the transition probability $K_k^{l-(m,n)}$. The label $[c_{m,n}]$ represents the energy region of the transition series concerning the $c_{m,n}$ subband. In this calculation, we take into account the lowest seven conduction subbands and 16 valence subbands.

In Fig. 4 the $c_{1,1}$-related transitions form the lowest two absorption peaks with different polarization dependence, whereas higher-energy absorption peaks are composed of the $c_{2,1}$-, $c_{1,2}$-, $c_{2,2}$-, $c_{3,1}$-, $c_{1,3}$-, and $c_{3,2}$-related transitions. First, we discuss the behaviors of the lowest two absorption peaks. In the nearly square QWR's with the cross-sectional ratio $L_x/L_z = 10/9$, in Fig. 4(a), the lowest-energy absorption peak is attributed to the v_1-$c_{1,1}$ transition having strong transition probability for mainly parallel polarization, whereas the second absorption peak due to the v_3-$c_{1,1}$ transition has transition probability only for perpendicular polarization. These two peaks exhibit a large transition strength and strong polarization anisotropy because the hh component and the lh component with the (1,1) envelope as well as the hh-lh mixing term are large in both the v_1 and v_3 subbands. With increasing cross-sectional ratio, the v_1-$c_{1,1}$ transition for perpendicular polarization increases and the v_3-$c_{1,1}$ transition decreases, whereas the v_1-$c_{1,1}$ transition for parallel polarization maintains almost the same transition probability. The small anisotropy at the v_1-$c_{1,1}$ transition, as shown in Fig. 4(d), is attributed to the reduced hh-lh mixing in the v_1 subband, indicating that the v_1 subband becomes hh-like in elongated QWR's. In addition to a reduction in the v_3-$c_{1,1}$ transition, an increase in the v_5-$c_{1,1}$ transition makes the second absorption peak broad and unclear. These results demonstrate that strong polarization anisotropy in the lowest two absorption peaks, which show the opposite polarization dependence, can be obtained only when the cross-sectional shape is nearly square.

It should be noted that transition properties of higher-energy transitions also depend on the cross-sectional ratio, reflecting the changes in the hh and lh components with higher (m,n) envelopes. However, it is difficult to distinguish the contribution of individual transitions to the change of the absorption spectra because various transitions energetically overlap. Here we describe the characters of only the $c_{2,1}$- and $c_{1,2}$-related transitions, where relatively-low-index valence subbands (v_2 and v_4) are dominantly concerned. According to the calculated results, the v_2-$c_{2,1}$ and v_4-$c_{2,1}$ transitions have transition probability mainly for parallel polarization, whereas the v_2-$c_{1,2}$ and v_4-$c_{1,2}$ transitions have

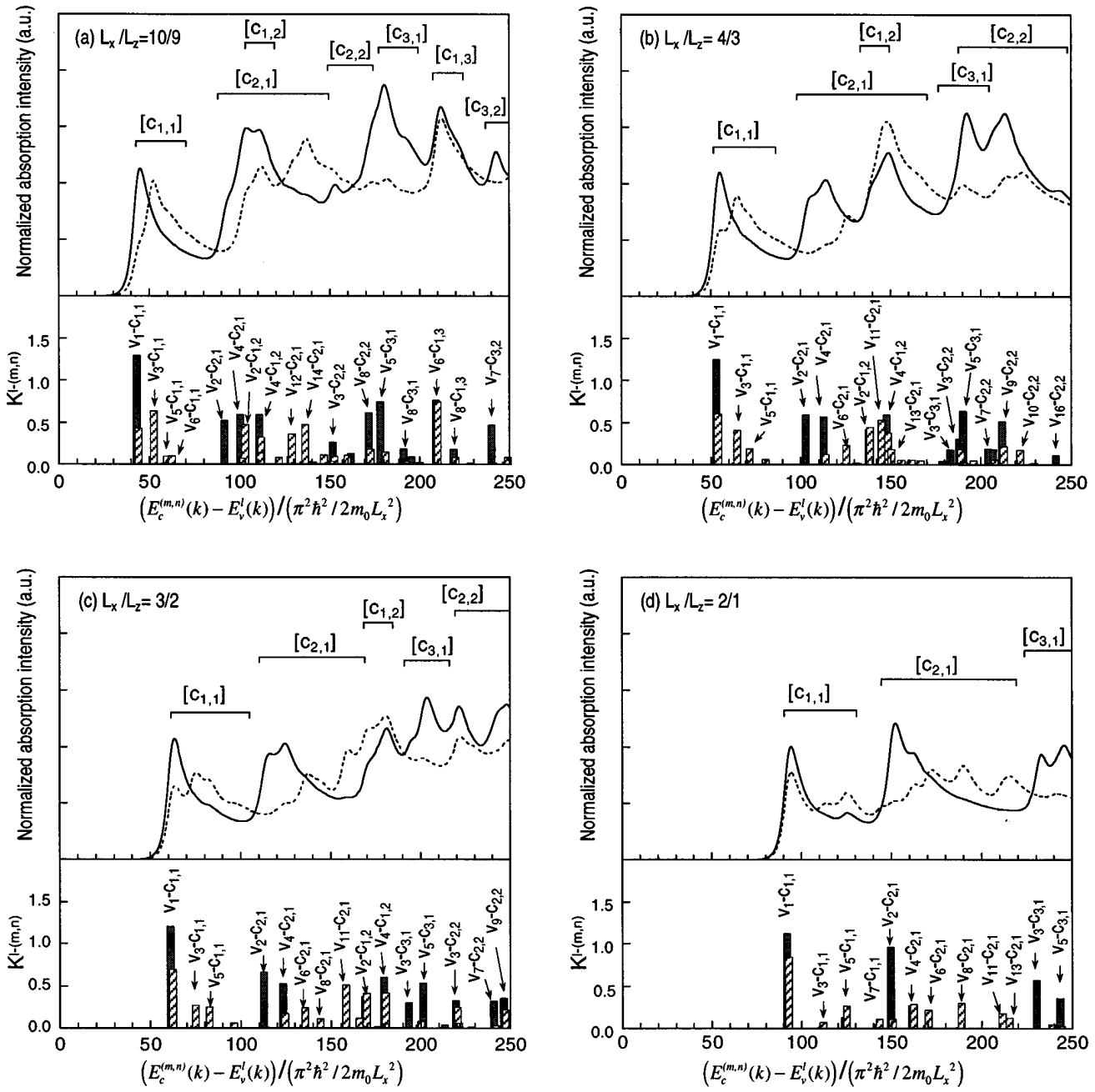

FIG. 4. Numerically calculated absorption spectra and values of $K_{k=0}^{l-(m,n)}$ at each transition edge ($k=0$) for rectangular QWR's with cross-sectional ratios of (a) $L_x/L_z=10/9$, (b) $L_x/L_z=4/3$, (c) $L_x/L_z=3/2$, and (d) $L_x/L_z=2/1$. The solid lines and dashed lines in the upper part of each figure represent the absorption spectra for incident polarization parallel and perpendicular to the wires, respectively. The horizontal axis is the sum of the conduction- and valence-subband confinement energies normalized by $\pi^2\hbar^2/2m_0L_x^2$. Solid (hatched) bars in the lower part of each figure show the values of $K_{k=0}^{l-(m,n)}$ for electric fields parallel (perpendicular) to the wires. The label v_l-$c_{m,n}$ denotes the transition between the v_l valence subband and the $c_{m,n}$ conduction subband with the (m,n) envelope.

transition probability for both polarizations. As shown in Fig. 4(a), the v_2-$c_{2,1}$ transition begins to increase absorption for parallel polarization at a normalized energy of 90 and the v_4-$c_{2,1}$, v_2-$c_{1,2}$, and v_4-$c_{1,2}$ transitions form the large third absorption peak for parallel polarization. The transition probability for perpendicular polarization in the v_2-$c_{1,2}$ and v_4-$c_{1,2}$ transitions also increases absorption around a normalized energy of 100 for perpendicular polarization. With an increase in the cross-sectional ratio, the energetic position of the $c_{1,2}$-related transition drastically increases because of the large energy shift of the $c_{1,2}$ subband. As a result, only the v_2-$c_{2,1}$ and v_4-$c_{2,1}$ transitions form the third absorption peak for parallel polarization. In the elongated QWR with $L_x/L_z=2$, as shown in Fig. 4(d), it should be noted that transition probability for parallel polarization of the v_2-$c_{2,1}$ transition at a normalized energy of 150 is highly enhanced, forming the prominent third absorption peak. In contrast to the smaller anisotropy in the v_1-$c_{1,1}$ transition, the third peak exhibits strong anisotropy, indicating strong hh-lh mixing with the (2,1) envelope in the v_2 subband. As explained ear-

lier, absorption spectra and polarization properties significantly vary with the cross-sectional ratio, especially around the lowest three absorption peaks.

C. Comparison of theory and experiment

Figures 5(a)–5(d) show the calculated absorption spectra for rectangular QWR's with (a) $L_x=21$ nm, $L_z=16.5$ nm; (b) $L_x=21$ nm, $L_z=13.5$ nm; (c) $L_x=21$ nm, $L_z=11$ nm; and (d) $L_x=17$ nm, $L_z=11$ nm. The vertical axis represents the absorption coefficient and the horizontal axis shows the transition energy at 15 K. These wire sizes were chosen to achieve the best fit with the lowest two PLE peaks measured for each sample. Here the homogeneous broadening of 6 meV at half-width at half maximum has been included by using a hyperbolic secant-type line-shape function. In the figures, the label $[c_{m,n}]$ denotes the conduction subband that mainly contributes to forming the absorption peak.

As for the lowest three PLE peaks, polarization anisotropy and the dependence of transition strength on the cross-sectional ratio (sizes) are well simulated by this theoretical calculation. With an increase in the cross-sectional ratio, the second absorption peak for perpendicular polarization broadens and the third absorption peak denoted by $[c_{2,1}]$ increases for parallel polarization, consistent with the experimental results. It is found that higher PLE peaks, including the third peaks in all samples, show a tendency to have lower quantized energies than the calculated peaks. This is because the electron wave functions in the higher conduction subbands penetrate into the barrier regions having finite potential height. However, the main features of the polarization properties are maintained because the penetration effects are weaker for the relatively-low-index valence subbands that dominantly determine the transition properties. Thus we can discuss qualitatively the polarization properties of the higher peaks based on the calculation.

In Fig. 3(a) the PLE spectrum for perpendicular polarization begins to increase around 1.59 eV, exhibits a shoulder structure around 1.62 eV, and gradually increases again above 1.63 eV, whereas the spectrum for parallel polarization has a small peak structure at 1.62 eV and increases drastically above 1.62 eV. Figure 3(b) also shows a similar spectra, i.e., the fourth peak (shoulder) appears around 1.64 eV for both polarizations and the PLE intensity increases above 1.66 eV for parallel polarization. According to the calculated transition probability in Figs. 4(b) and 4(c), $c_{2,1}$-related transitions, such as v_6-$c_{2,1}$, v_8-$c_{2,1}$, v_{11}-$c_{2,1}$, and v_{13}-$c_{2,1}$ transitions, contribute to increasing absorption for perpendicular polarization, whereas the v_2-$c_{1,2}$ and v_4-$c_{1,2}$ transitions cause absorption for both polarizations. It should also be noted that the $c_{3,1}$- and $c_{2,2}$-related transitions have large transition probability for mainly parallel polarization, forming absorption peaks in the higher-energy side of the $c_{2,1}$- and $c_{1,2}$-related transitions. Thus the fourth peaks (shoulders) and the increase of PLE intensity above the fourth peaks are attributed to the $c_{1,2}$-related transitions and to the $c_{3,1}$- and $c_{2,2}$-related transitions, respectively. As for sample 3, the calculation reproduces well the PLE spectra around the lowest three peaks for both polarizations. The featureless PLE spectra in the higher-energy side of the third

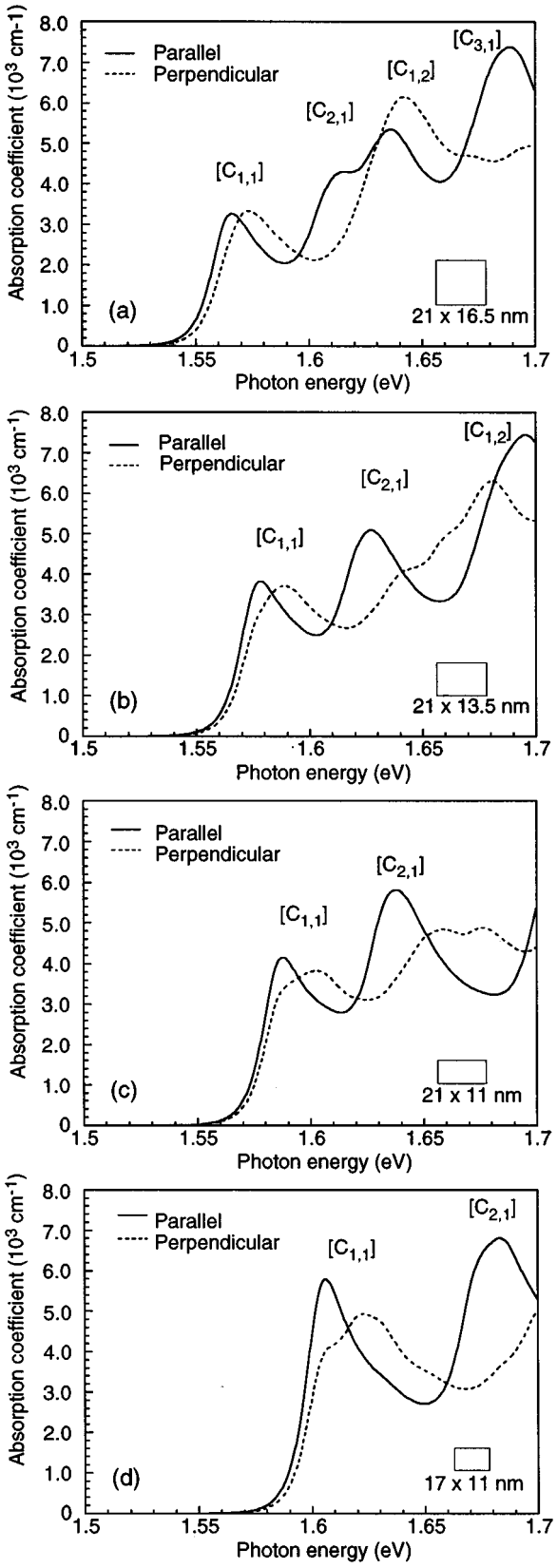

FIG. 5. Calculated absorption spectra for rectangular QWR's with (a) $L_x=21$ nm, $L_z=16.5$ nm; (b) $L_x=21$ nm, $L_z=13.5$ nm; (c) $L_x=21$ nm, $L_z=11$ nm; and (d) $L_x=17$ nm, $L_z=11$ nm. The vertical axis represents the absorption coefficient and the horizontal axis shows the transition energy at 15 K. The label $[c_{m,n}]$ denotes the indices of the transition series.

peak are attributed to wide subband energy separation in the thin QWR's. As discussed above, the experimental results are well explained by the theoretical calculation, clarifying the polarization properties and the cross-sectional shape dependence of the lowest several absorption peaks in rectangular GaAs QWR's. These results clearly confirm the formation of 1D valence-subband structures, which significantly vary depending on the quantum confinement conditions in QWR's.

V. CONCLUSION

In summary, we studied experimentally and theoretically the interband optical transition spectra of GaAs/AlAs rectangular QWR's of various wire sizes. The high-quality GaAs QWR's with lateral sizes below 20 nm were achieved by MOCVD growth on nonplanar substrates. Experiments demonstrated that the polarization properties of the PLE spectra, which have several clear peaks corresponding to the optical transitions between quantized conduction and valence subbands, significantly depend on the cross-sectional ratios of the rectangular wires. The polarization-dependent transition matrix element and the detailed absorption spectra of the QWR's with rectangular cross sections were calculated by taking into account hh and lh mixing in 1D valence subbands and their dispersion properties. The theoretical results clarify the physical origin of the PLE peaks. They also explain well the dependence of the transition strength and polarization anisotropy on the wire cross-sectional shapes as to the lowest three or four PLE peaks. It was demonstrated experimentally and theoretically that the characteristics of the 1D valence subbands depend significantly on the quantum confinement conditions, i.e., on the relative confinement strength between two spatial directions. In the present study, 1D excitonic effects distinctive from interband optical transitions were not clearly observed. It was indistinguishable whether the impurity effects prevented the formation of excitonic states or inhomogeneous broadening concealed the excitonic features. Further improvements in the fabrication technique, such as precise control of wire sizes and shapes as well as a reduction in residual impurity, are necessary to allow the more detailed optical properties of 1D excitons to be investigated.[12,31,41,42]

ACKNOWLEDGMENTS

We would like to thank Dr. Tadashi Saitoh and Hideki Gotoh for their fruitful discussions and technical assistance with the fabrication and we gratefully acknowledge the help we received in discussions with Dr. Naoki Kobayashi and Dr. Arturo Chavez-Pirson.

*FAX: 81-462-40-4713. Electronic address: sogawa@will.brl.ntt.co.jp

[1] H. Sakaki, Jpn. J. Appl. Phys. **19**, L735 (1980).
[2] Y. Arakawa and H. Sakaki, Appl. Phys. Lett. **40**, 939 (1982).
[3] K. Kash, A. Scherer, J. M. Worlock, H. G. Craighead, and M. C. Tamargo, Appl. Phys. Lett. **49**, 1043 (1986).
[4] M. Notomi, M. Okamoto, H. Iwamura, and T. Tamamura, Appl. Phys. Lett. **62**, 1094 (1993).
[5] E. Kapon, M. C. Tamargo, and D. M. Hwang, Appl. Phys. Lett. **50**, 347 (1987).
[6] E. Kapon, D. M. Hwang, and R. Bhat, Phys. Rev. Lett. **63**, 430 (1989).
[7] E. Kapon, K. Kash, E. M. Clausen, Jr., D. M. Hwang, and E. Colas, Appl. Phys. Lett. **60**, 477 (1992).
[8] S. Koshiba, H. Noge, H. Akiyama, T. Inoshita, Y. Nakamura, A. Shimizu, Y. Nagamune, M. Tsuchiya, H. Kano, and H. Sakaki, Appl. Phys. Lett. **64**, 363 (1994).
[9] E. Kapon, G. Biasiol, D. M. Hwang, and E. Colas, Microelectron. J. **26**, 881 (1995).
[10] S. Tsukamoto, Y. Nagamune, M. Nishioka, and Y. Arakawa, J. Appl. Phys. **71**, 533 (1992).
[11] H. Saito, K. Uwai, and N. Kobayashi, Jpn. J. Appl. Phys. 1 **32**, 4440 (1993).
[12] H. Ando, H. Saito, A. Chavez-Pirson, H. Gotoh, and N. Kobayashi, Appl. Phys. Lett. **69**, 1512 (1996).
[13] K. Y. Cheng, K. C. Hsieh, and N. Baillargeon, Appl. Phys. Lett. **60**, 2892 (1992).
[14] A. C. Chen, A. M. Moy, P. J. Pearah, K. C. Hsieh, and K. Y. Cheng, Appl. Phys. Lett. **62**, 1359 (1993).
[15] D. Gershoni, J. S. Weiner, S. N. G. Chu, G. A. Baraff, J. M. Vandenberg, L. N. Pfeiffer, K. West, R. A. Logan, and T. Tanbun-Ek, Phys. Rev. Lett. **65**, 1631 (1990).
[16] A. R. Goni, L. N. Pfeiffer, K. W. West, A. Pinczuk, H. U. Baranger, and H. L. Stormer, Appl. Phys. Lett. **61**, 1956 (1992).
[17] M. Krishnamurthy, M. Wassermeier, D. R. M. Williams, and P. M. Petoff, Appl. Phys. Lett. **62**, 1922 (1993).
[18] D. Leonard, M. Krishnamurthy, C. M. Reaves, S. P. Denbaars, and P. M. Petoff, Appl. Phys. Lett. **63**, 3203 (1993).
[19] N. Carlsson, W. Seifert, A. Petersson, P. Castrillo, M.-E. Pistol, and L. Samuelson, Appl. Phys. Lett. **65**, 3093 (1994).
[20] D. Hessman, P. Castrillo, M.-E. Pistol, C. Pryor, and L. Samuelson, Appl. Phys. Lett. **69**, 749 (1996).
[21] T. Sogawa, S. Ando, and H. Kanbe, Appl. Phys. Lett. **64**, 472 (1994).
[22] T. Sogawa, S. Ando, and H. Kanbe, Appl. Phys. Lett. **64**, 3299 (1994).
[23] T. Sogawa, S. Ando, and H. Kanbe, Appl. Phys. Lett. **67**, 1087 (1995).
[24] T. Sogawa, S. Ando, and H. Kanbe, Jpn. J. Appl. Phys. 1 **34**, 4405 (1995).
[25] T. Sogawa, S. Ando, H. Ando, and H. Kanbe, Appl. Phys. Lett. **68**, 364 (1996).
[26] J. A. Brum, G. Bastard, L. L. Chang, and L. Esaki, Superlattices Microstruct. **3**, 47 (1987).
[27] J. A. Brum and G. Bastard, Superlattices Microstruct. **4**, 443 (1988).
[28] D. S. Citrin and Y.-C. Chang, Phys. Rev. B **40**, 5507 (1989).
[29] U. Bockelmann and G. Bastard, Phys. Rev. B **45**, 1688 (1992).
[30] P. C. Sercel and K. J. Vahala, Phys. Rev. B **44**, 5681 (1991).
[31] H. Ando, S. Nojima, and H. Kanbe, J. Appl. Phys. **74**, 6383 (1993).
[32] H. Ando, A. Chavez-Pirson, H. Saito, and H. Kanbe, J. Appl. Phys. **77**, 3372 (1995).
[33] G. Goldoni and A. Fasolino, Phys. Rev. B **52**, 14 118 (1995).
[34] G. Goldoni, F. Rossi, E. Molinari, A. Fasolino, R. Rinaldi, and R. Cingolani, Appl. Phys. Lett. **69**, 2965 (1996).

[35] T. Sogawa, S. Ando, H. Ando, and H. Kanbe (unpublished).
[36] M. H. Degani and O. Hipolito, Phys. Rev. B **35**, 9345 (1987).
[37] P. Christol, P. Lefebvre, and H. Mathieu, J. Appl. Phys. **74**, 5626 (1993).
[38] T. Ogawa and T. Takagahara, Surf. Sci. **263**, 506 (1992).
[39] J. M. Luttinger and W. Kohn, Phys. Rev. **97**, 869 (1955).
[40] G. D. Sanders and Y.-C. Chang, Phys. Rev. B **32**, 5517 (1985).
[41] F. Rossi and E. Molinari, Phys. Rev. Lett. **76**, 3642 (1996).
[42] F. Rossi and E. Molinari, Phys. Rev. B **53**, 16 462 (1996).